

PROPERTIES OF NEUTRINO-DRIVEN EJECTA FROM THE REMNANT OF BINARY NEUTRON STAR MERGER : PURELY RADIATION HYDRODYNAMICS CASE

SHO FUJIBAYASHI

Department of Physics, Graduate School of Science, Kyoto University, Kyoto 606-8502, Japan

YUICHIRO SEKIGUCHI

Department of Physics, Toho University, Funabashi, Chiba 274-8510, Japan

KENTA KIUCHI AND MASARU SHIBATA

Center for Gravitational Physics, Yukawa Institute for Theoretical Physics, Kyoto University, Kyoto 606-8502, Japan

Draft version July 20, 2022

ABSTRACT

We performed general relativistic, long-term, axisymmetric neutrino radiation hydrodynamics simulations for the remnant formed after the binary neutron star merger, which consist of a massive neutron star and a surrounding torus. We investigate the properties of neutrino-driven ejecta. As an initial condition, we employ the result derived in a three-dimensional, numerical relativity simulation for the binary neutron star merger. Due to the pair-annihilation heating, the dynamics of the neutrino-driven ejecta is significantly modified. The kinetic energy of the ejecta is about two times larger than that in the result without the pair-annihilation heating. This suggests that the pair-annihilation heating plays an important role in the evolution of the merger remnants. The relativistic outflow, which is required for driving gamma-ray bursts, is not observed because the specific heating rate around the rotational axis is not sufficiently high. This is caused by the baryon loading due to the neutrino-driven ejecta from the massive neutron star itself. We discuss the condition for launching the relativistic outflow and the nucleosynthesis in the ejecta.

Keywords: accretion, accretion disks–neutrinos–stars: neutron–gamma-ray burst: general–relativistic processes

1. INTRODUCTION

Binary neutron star (NS-NS) merger is one of the promising sources of gravitational waves for ground-based gravitational-wave detectors, such as advanced LIGO, advanced Virgo, and KAGRA (Abadie et al. 2010; Accadia et al. 2011; Kuroda & LCGT Collaboration 2010). In association with gravitational waves, the merger remnant, which is composed of a central compact object (NS or black hole) surrounded by a massive accretion torus, emits a huge amount of neutrinos. Neutrinos emitted could be a major source of various types of phenomena as follows.

First, a large amount of mass could be ejected as sub-relativistic neutrino-driven wind, in addition to the dynamical mass ejection, which would occur at NS-NS mergers (Dessart et al. 2009; Metzger & Fernández 2014; Perego et al. 2014). Then, a substantial amount of radioactive nuclei are likely to be synthesized via the rapid neutron-capture process, the so-called *r*-process (Lattimer & Schramm 1974; Symbalisty & Schramm 1982; Eichler et al. 1989; Rosswog et al. 1999; Freiburghaus et al. 1999; Goriely et al. 2011; Wanajo et al. 2014). The ejecta is heated by the radioactive decay of these heavy elements and would shine at optical and infra-red band in 1–10 days after the merger (Li & Paczyński 1998; Kasen et al. 2013; Tanaka & Hotokezaka 2013). Simultaneous detection of this so-called “kilonova” or “macronova” with gravitational waves will significantly improve po-

sitional accuracy of gravitational wave sources. The neutrino-driven ejecta could be an additional energy source to the dynamical ejecta.

Second, if a relativistic outflow is launched by neutrino heating, the merger remnant would drive short-duration gamma-ray bursts (SGRBs). The pair-annihilation process of neutrinos and anti-neutrinos is important for the extremely relativistic ejecta (Eichler et al. 1989; Meszaros & Rees 1992; Narayan et al. 1992). This is because this process can deposit the energy into materials regardless of the baryon density, so that the ejecta achieve large photon-to-baryon ratio if the density is sufficiently low in the heating region. We should note that there are several other scenarios proposed to drive the relativistic ejecta, such as the electromagnetic energy extractions from rotating black-holes (Blandford & Znajek 1977) and pulsars (Usov 1992).

Radiation hydrodynamics simulations of the merger-remnant torus surrounding a central object have been performed by many authors (Dessart et al. 2009; Fernandez et al. 2013; Metzger & Fernández 2014; Perego et al. 2014; Fernández et al. 2015; Just et al. 2016; Foucart et al. 2016). Recently, simulations of black hole-torus system approximately taking the pair-annihilation heating into account were performed (Just et al. 2016). It was concluded that the system is unlikely to drive SGRBs because the neutrino heating cannot overcome the mass loading.

Recent numerical relativity simulations of the NS-NS mergers with finite-temperature equations of state (EOS)

that can support the observed $\sim 2M_\odot$ NSs (Demorest et al. 2010; Antoniadis et al. 2013) have suggested that a massive neutron star (MNS) is likely to be formed as the remnant of the merger if the total binary mass is not extremely high ($\lesssim 2.8M_\odot$) (Shibata et al. 2005; Shibata & Taniguchi 2006; Kiuchi et al. 2009, 2010; Sekiguchi et al. 2011; Hotokezaka et al. 2011, 2013; Kaplan et al. 2014; Takami et al. 2015; Dietrich et al. 2015). The structure of the neutrino emissivity of the MNS-torus system is quite different from that of the black-hole-torus system. The MNS itself emits a large amount of neutrinos. In addition, the torus matter does not accrete into the black-hole, but stops at the surface of the MNS. Such an inner region of the torus significantly contributes to the neutrino emission. Therefore, if the lifetime of MNSs is sufficiently long, a huge influence of neutrinos on the ejecta is expected. Recent numerical relativity simulations for the NS-NS mergers (Sekiguchi et al. 2015, 2016) showed that the effect of neutrino irradiation is significant near the rotational axis. However, their simulation time is not so long as the accretion time of the torus ($\gtrsim 100$ ms). Hence, to explore the entire effects of neutrinos a longer-term simulation is required.

In Richers et al. (2015), the pair-annihilation heating rate in a MNS-torus system was calculated with a Monte-Carlo method using snapshots of the pseudo-Newtonian hydrodynamics simulations (Metzger & Fernández 2014) as their background configurations. Perego et al. (2017) also calculated the heating rate with a ray-tracing method as a post process of the Newtonian hydrodynamics simulations for the NS-NS merger (Perego et al. 2014). It was suggested that the total energy deposited by the pair-annihilation heating is not large enough to account for the typical energy of observed SGRB events, although the presence of the MNS does increase the pair-annihilation rate. Perego et al. (2017) concluded that much larger neutrino luminosities are required to explain most of the observed SGRBs. Compared with the Newtonian simulation, however, the merger becomes more violent in simulations with general relativity because of the deeper potential well. Hence, the temperature of the merger remnant becomes higher than that with Newtonian gravity. Therefore, their Newtonian simulation may underestimate the neutrino luminosity. Moreover, Perego et al. (2017) employed a stiff EOS, referred to as TM1 (Hempel et al. 2012), so that the neutrino luminosity is lower than that with softer EOSs. We can expect that the neutrino pair-annihilation heating will be more efficient in the general relativistic simulation with softer EOS.

Motivated by the above considerations, in this paper, we investigate the neutrino-driven ejecta from the MNS-torus system. We perform long-term fully general relativistic simulations with an approximate neutrino radiation transport in axial symmetry using the initial condition based on a three-dimensional numerical relativity merger simulation. We also investigate the effects of the neutrino-antineutrino pair-annihilation heating, which is not taken into account in our previous studies (Sekiguchi et al. 2015, 2016). The outline of this paper is as follows. A brief description of the simulation setting and the initial condition which we employ are given in Sec. 2. Then, the results of the simulations are presented in Sec. 3. Finally, discussions and the conclusions are given in Secs. 4

and 5, respectively. Throughout this paper, we use the units of $c = 1 = G$, where c and G are the speed of light and the gravitational constant, respectively.

2. METHOD

2.1. Einstein's Equation

In our simulation, Einstein's equation is solved in the Baumgarte-Shapiro-Shibata-Nakamura (BSSN)-puncture formalism (Shibata & Nakamura 1995; Baumgarte & Shapiro 1999; Campanelli et al. 2006). In this formalism, we evolve the conformal three-metric $\tilde{\gamma}_{ij} = \gamma^{-1/3}\gamma_{ij}$, the conformal factor $W = \gamma^{-1/6}$ (Marronetti et al. 2008), the trace of the extrinsic curvature $K = \gamma^{ij}K_{ij}$, the trace-free part of the extrinsic curvature $\tilde{A}_{ij} = \gamma^{-1/3}(K_{ij} - \gamma_{ij}K/3)$, and the auxiliary variable $F_i = \partial_k \tilde{\gamma}_{ki}$. Here, $\gamma_{\alpha\beta} = g_{\alpha\beta} + n_\alpha n_\beta$ is the induced metric, where $g_{\alpha\beta}$ and n_α are the spacetime metric and the timelike unit vector normal to the time slice, respectively, $\gamma = \det(\gamma_{ij})$, and $\det(\tilde{\gamma}_{ij})$ is assumed to be unity. We adopt the so-called cartoon method (Alcubierre et al. 2001; Shibata 2003a) to impose axially symmetric conditions for the geometric quantities. We evaluate the spatial derivative by a fourth-order central finite difference. We add a sixth order Kreiss-Oliger-type dissipation terms (Brügmann et al. 2008) to the evolution equations of the geometrical variables in order to improve non-linear stability of this scheme. For the gauge condition, we adopt dynamical lapse (Alcubierre et al. 2003) and shift (Shibata 2003b) conditions as

$$\partial_t \alpha = -2\alpha K, \quad (1)$$

$$\partial_t \beta^i = \frac{3}{4} \tilde{\gamma}^{ij} (F_j + \partial_t F_j \Delta t), \quad (2)$$

where α and β_i is the lapse function and the shift vector, respectively, and Δt is the time-step interval.

2.2. Neutrino-radiation Hydrodynamics Equations

We implement the so-called M1-closure scheme based on Thorne's moment formalism for neutrino-radiation transport (Thorne 1981; Shibata et al. 2011). In addition, we estimate the source term for the neutrino transfer based on a leakage-based scheme (for the leakage scheme, see, e.g., Cooperstein 1988). Here we give a brief description of our formulation. In this work, we consider three species of neutrinos: electron neutrinos ν_e , electron antineutrinos $\bar{\nu}_e$, and the other neutrino species ν_x , which represents all of the heavy-lepton neutrinos ν_μ , $\bar{\nu}_\mu$, ν_τ , and $\bar{\nu}_\tau$.

The basic equation of the fluid is derived from the energy-momentum conservation equation. On the other hand, the basic equation of the neutrinos is the energy-integrated, first moment of the Boltzmann equation. They are written, respectively, as

$$\nabla_\beta T_{(\text{fluid})}^{\alpha\beta} = -Q^\alpha = -\sum_i Q_{\nu_i}^\alpha, \quad (3)$$

$$\nabla_\beta T_{(\nu_i)}^{\alpha\beta} = Q_{\nu_i}^\alpha, \quad (4)$$

where $T_{(\text{fluid})}^{\alpha\beta}$ and $T_{(\nu_i)}^{\alpha\beta}$ are the energy-momentum tensors of the fluid and the i -th species of neutrinos, respectively, and $Q_{\nu_i}^\alpha$ is the energy-momentum source term

of the i -th species of neutrinos, which is determined by weak-interaction processes. Here, the total energy-momentum tensor is $T_{(\text{tot})}^{\alpha\beta} = T_{(\text{fluid})}^{\alpha\beta} + \sum_i T_{(\nu_i)}^{\alpha\beta}$, which satisfies $\nabla_\beta T_{(\text{tot})}^{\alpha\beta} = 0$.

In our scheme, the energy-momentum tensor of neutrinos is phenomenologically decomposed as

$$T_{(\nu_i)}^{\alpha\beta} = T_{(\nu_i, \text{T})}^{\alpha\beta} + T_{(\nu_i, \text{S})}^{\alpha\beta}, \quad (5)$$

where $T_{(\nu_i, \text{T})}^{\alpha\beta}$ and $T_{(\nu_i, \text{S})}^{\alpha\beta}$ are the contributions of “trapped-” and “streaming-” neutrinos, respectively. We assume that a part of neutrinos produced at a rate $Q_{\nu_i}^\alpha$ becomes streaming-neutrinos at a leakage rate $Q_{(\text{leak})\nu_i}^\alpha$ (for the detail of this term, see Sekiguchi et al. 2012), and the other part becomes trapped-neutrinos at a rate $Q_{\nu_i}^\alpha - Q_{(\text{leak})\nu_i}^\alpha$.

We assume that trapped-neutrinos are tightly coupled with the fluid. Then the energy-momentum tensor of trapped-neutrinos can be written by that of the fluid of relativistic Fermi particles, and thus, we decompose the

total energy-momentum tensor as

$$T_{(\text{tot})}^{\alpha\beta} = T^{\alpha\beta} + \sum_i T_{(\nu_i, \text{S})}^{\alpha\beta}, \quad (6)$$

where $T^{\alpha\beta} = T_{(\text{fluid})}^{\alpha\beta} + \sum_i T_{(\nu_i, \text{T})}^{\alpha\beta}$ is the energy-momentum tensor composed of the sum of the fluid and trapped-neutrinos. It is written in the form

$$T_{\alpha\beta} = \rho h u_\alpha u_\beta + P g_{\alpha\beta}. \quad (7)$$

Here ρ is the baryon rest-mass density, u^α is the four-velocity of the fluid, $h = 1 + \varepsilon + P/\rho$ is the specific enthalpy, P is the pressure, and ε is the specific internal energy. P and ε contain the contributions from baryons, electrons, positrons, and trapped-neutrinos.

We evolve the fluid variables in cylindrical coordinates (R, φ, z) . Hereafter, we regard the $y = 0$ plane of Cartesian coordinates (x, y, z) as a meridional ($\varphi = 0$) plane of cylindrical coordinates (R, φ, z) . The Euler and energy equations can be written, respectively, as

$$\partial_t(\rho_* \hat{e}) + \frac{1}{x} \partial_k [x(\rho_* \hat{e} v^k + W^{-3} P(v^k + \beta^k))] = \alpha \left[W^{-3} S_{kl} K^{kl} - \gamma^{kl} \rho_* \hat{u}_k \partial_l \ln \alpha + W^{-3} Q_{(\text{leak})}^\alpha n_\alpha \right], \quad (8)$$

$$\partial_t(\rho_* \hat{u}_i) + \frac{1}{x} \partial_k [x(\rho_* \hat{u}_i v^k + \alpha W^{-3} P \delta^k_i)] = \alpha \left[-\rho_* \hat{e} \partial_i \ln \alpha + \frac{1}{\alpha} \rho_* \hat{u}_k \partial_i \beta^k + \frac{1}{2} W^{-3} S_{kl} \partial_i \gamma^{kl} - W^{-3} Q_{(\text{leak})}^\alpha \gamma_{\alpha i} \right], \quad (9)$$

where $\rho_* = W^{-3} w \rho$, $\hat{u}_i = h u_i$, $v^i = u^i / u^t$, $\hat{e} = h w - P / (w \rho)$, $S_{ij} = T_{\alpha\beta} \gamma^\alpha_i \gamma^\beta_j = \rho h u_i u_j + P \gamma_{ij}$, $w \equiv -n_\alpha u^\alpha = \sqrt{1 + \gamma^{ij} u_i u_j}$ is the Lorentz factor of the fluid, and $Q_{(\text{leak})}^\alpha$ is the sum of leakage source terms of all neutrino species.

In order to evaluate the pressure and the internal energy, the number density of baryons, electrons, and trapped-neutrinos is evolved by

$$\nabla_\alpha(\rho u^\alpha) = 0, \quad (10)$$

$$\nabla_\alpha(\rho Y_e u^\alpha) = \mathcal{R}_e, \quad (11)$$

$$\nabla_\alpha(\rho Y_{\nu_i} u^\alpha) = \mathcal{R}_{\nu_i} - \mathcal{R}_{(\text{leak})\nu_i}, \quad (12)$$

where \mathcal{R}_e and \mathcal{R}_{ν_i} denote the source terms for the number evolution of leptons due to the weak interactions. Here we assumed that a part of neutrinos produced at a rate \mathcal{R}_{ν_i} becomes trapped-neutrinos at a rate $\mathcal{R}_{\nu_i} - \mathcal{R}_{(\text{leak})\nu_i}$, where $\mathcal{R}_{(\text{leak})\nu_i}$ is the number emission rate of neutrinos of the flavor i due to the diffusion (for the details, see Sekiguchi et al. 2012). Eqs. (10)–(12) are

written in the following forms, respectively;

$$\partial_t \rho_* + \frac{1}{x} \partial_k (x \rho_* v^k) = 0, \quad (13)$$

$$\partial_t(\rho_* Y_e) + \frac{1}{x} \partial_k (x \rho_* Y_e v^k) = \alpha W^{-3} \mathcal{R}_e, \quad (14)$$

$$\partial_t(\rho_* Y_{\nu_i}) + \frac{1}{x} \partial_k (x \rho_* Y_{\nu_i} v^k) = \alpha W^{-3} (\mathcal{R}_{\nu_i} - \mathcal{R}_{(\text{leak})\nu_i}). \quad (15)$$

For streaming-neutrinos, we decompose their energy-momentum tensor as

$$T_{(\nu_i, \text{S})\alpha\beta} = E n_\alpha n_\beta + F_\alpha n_\beta + F_\beta n_\alpha + P_{\alpha\beta}, \quad (16)$$

where $E = T_{(\text{S})\mu\nu} n^\mu n^\nu$, $F_\alpha = -T_{(\text{S})\mu\nu} \gamma^\mu_\alpha n^\nu$, and $P_{\alpha\beta} = T_{(\text{S})\mu\nu} \gamma^\mu_\alpha \gamma^\nu_\beta$ are the energy density, energy flux, and spatial stress tensor of streaming-neutrinos, respectively, which satisfy $F_\alpha n^\alpha = P_{\alpha\beta} n^\alpha = 0$. Here we omit the subscripts of the species of neutrinos. The evolution equations for E and F_i are

$$\partial_t \tilde{E} + \frac{1}{x} \partial_k [x(\alpha \tilde{F}^k - \beta^k \tilde{E})] = \alpha [\tilde{F}^{kl} K_{kl} - \tilde{F}^k \partial_k \ln \alpha - W^{-3} Q_{(\text{leak})}^\alpha n_\alpha], \quad (17)$$

$$\begin{aligned} \partial_t \tilde{F}_i + \frac{1}{x} \partial_k [x(\alpha \tilde{P}_i^k - \beta^k \tilde{F}_i)] = & \alpha \left[-\tilde{E} \partial_i \ln \alpha + \frac{1}{\alpha} \tilde{F}_k \partial_i \beta^k \right. \\ & \left. + \frac{1}{2} \tilde{P}^{kl} \partial_i \gamma_{kl} + W^{-3} Q_{(\text{leak})}^\alpha \gamma_{\alpha i} \right], \end{aligned} \quad (18)$$

where $\tilde{E} = W^{-3} E$, $\tilde{F}_i = W^{-3} F_i$, and $\tilde{P}^{ij} = W^{-3} P^{ij}$. In order to determine P^{ij} , we use the so-called M1-closure relation (Levermore 1984; González et al. 2007). In this closure relation, the spatial stress tensor is written as

$$P^{ij} = \frac{3\chi - 1}{2} (P^{ij})_{\text{thin}} + \frac{3(1 - \chi)}{2} (P^{ij})_{\text{thick}}, \quad (19)$$

where $(P^{ij})_{\text{thin}}$ and $(P^{ij})_{\text{thick}}$ are the spatial stress tensor in the optically thin and thick limits, respectively, which are written as

$$(P^{ij})_{\text{thin}} = E \frac{F^i F^j}{\gamma_{kl} F^k F^l}, \quad (20)$$

$$\begin{aligned} (P^{ij})_{\text{thick}} = & \frac{E}{2w^2 + 1} [(2w^2 - 1)\gamma^{ij} - 4V^i V^j] \\ & + \frac{1}{w} [F^i V^j + F^j V^i] \\ & + \frac{2F^k u_k}{w(2w^2 + 1)} [-w^2 \gamma^{ij} + V^i V^j], \end{aligned} \quad (21)$$

where $V^i = \gamma^{ij} u_j$ (Shibata et al. 2011). χ is the so-called variable Eddington factor, which is a function of a normalized flux $f^2 = h_{\alpha\beta} H^\alpha H^\beta / J^2$ and we choose the following form:

$$\chi = \frac{3 + 4f^2}{5 + 2\sqrt{4 - 3f^2}}. \quad (22)$$

Here we define the energy density J , energy flux H^α , and spatial stress-tensor $L^{\alpha\beta}$ of streaming-neutrinos in the fluid rest frame by $J = T_{(S)}^{\alpha\beta} u_\alpha u_\beta$, $H^\alpha = -T_{(S)}^{\gamma\beta} u_\beta h^\alpha_\gamma$, and $L^{\alpha\beta} = T_{(S)}^{\gamma\delta} h^\alpha_\gamma h^\beta_\delta$, respectively, where $h_{\alpha\beta} = g_{\alpha\beta} + u_\alpha u_\beta$ is a projection operator.

2.3. Microphysics

2.3.1. Equation of State

In this paper, for the nuclear equation of state (EOS), we adopt a tabulated EOS referred to as DD2 (Banik et al. 2014), which is the same EOS as one of adopted in a three-dimensional simulation for the NS-NS merger (Sekiguchi et al. 2015). The remnant of the NS-NS merger of the typical neutron-star mass ($1.3 - 1.4M_\odot$) is a long-lived MNS, and hence, we can explore the long-term phenomena associated with the MNS surrounded by a torus.

The original table of the EOS covers only ranges of density $10^{3.2} - 10^{16.2} \text{ g cm}^{-3}$ and temperature $10^{-1} - 10^{2.2} \text{ MeV}$, but the density and the temperature of the ejecta become lower than the lowest values of the table. In order to treat such a low density and temperature regions,

we extend the table to ranges with $10^{-0.8} - 10^{16.2} \text{ g cm}^{-3}$ and $10^{-3} - 10^{2.2} \text{ MeV}$ using an EOS by Timmes & Swesty (2000). This EOS includes contributions of nucleons, heavy nuclei, electrons, positrons and photons to the pressure and the internal energy.

2.3.2. Weak Interaction

The source terms of Eqs. (3) and (4) are

$$\begin{aligned} Q_{\nu_e}^\alpha = & \left(Q_{\text{brems},\nu_e}^{(-)} + Q_{\text{pair},\nu_e}^{(-)} + Q_{\text{plasm},\nu_e}^{(-)} + Q_{\text{ec}}^{(-)} \right) u^\alpha \\ & - Q_{\text{pair},\nu_e}^{(+)\alpha} - Q_{\text{abs},\nu_e}^{(+)\alpha}, \end{aligned} \quad (23)$$

$$\begin{aligned} Q_{\bar{\nu}_e}^\alpha = & \left(Q_{\text{brems},\bar{\nu}_e}^{(-)} + Q_{\text{pair},\bar{\nu}_e}^{(-)} + Q_{\text{plasm},\bar{\nu}_e}^{(-)} + Q_{\text{pc}}^{(-)} \right) u^\alpha \\ & - Q_{\text{pair},\bar{\nu}_e}^{(+)\alpha} - Q_{\text{abs},\bar{\nu}_e}^{(+)\alpha}, \end{aligned} \quad (24)$$

$$\begin{aligned} Q_{\nu_x}^\alpha = & \left(Q_{\text{brems},\nu_x}^{(-)} + Q_{\text{pair},\nu_x}^{(-)} + Q_{\text{plasm},\nu_x}^{(-)} \right) u^\alpha \\ & - Q_{\text{pair},\nu_x}^{(+)\alpha}. \end{aligned} \quad (25)$$

Here, $Q_{\text{brems},\nu_i}^{(-)}$, $Q_{\text{pair},\nu_i}^{(-)}$, $Q_{\text{plasm},\nu_i}^{(-)}$, $Q_{\text{pc}}^{(-)}$, and $Q_{\text{ec}}^{(-)}$ are the neutrino cooling (emission) rates due to the nucleon-nucleon Bremsstrahlung, the electron-positron pair-annihilation, the plasmon decay, the electron-capture, and the positron-capture processes, respectively. On the other hand, $Q_{\text{pair},\nu_i}^{(+)\alpha}$, $Q_{\text{abs},\nu_e}^{(+)\alpha}$, and $Q_{\text{abs},\bar{\nu}_e}^{(+)\alpha}$ are the matter-heating source terms due to the neutrino-antineutrino pair-annihilation, the electron-neutrino and electron-antineutrino absorption processes, respectively. For electron and positron capture processes, we use the rate in Fuller et al. (1985). On the other hand, for pair-production processes, we use the rates in Cooperstein et al. (1986) for electron-positron pair-annihilation, Ruffert et al. (1996) for plasmon-decay, and Burrows et al. (2006) for nucleon-nucleon Bremsstrahlung, respectively. Except for the neutrino pair-annihilation process, the rates adopted in the present simulations are the same as those adopted in the simulations for three-dimensional NS-NS merger (Sekiguchi et al. 2015). The explicit forms of the cooling rates ($Q_{\text{brems},\nu_i}^{(-)}$, $Q_{\text{pair},\nu_i}^{(-)}$, $Q_{\text{plasm},\nu_i}^{(-)}$, $Q_{\text{pc}}^{(-)}$, and $Q_{\text{ec}}^{(-)}$) are found in Sekiguchi et al. (2012).

The source term due to the neutrino pair-annihilation process is written (in $\hbar = 1$ unit) as

$$\begin{aligned} Q_{\text{pair},\nu_i}^{(+)\alpha} = & \left[\frac{C_{\nu_i \bar{\nu}_i}^{\text{pair}} G_{\text{F}}^2}{3\pi} \langle \omega \rangle_{\text{pair}} (J\bar{J} - 2H^\beta \bar{H}_\beta + L^{\beta\gamma} \bar{L}_{\beta\gamma}) e^{-\tau_{\nu_i}} \right] u^\alpha \\ = & Q_{\text{pair},\nu_i}^{(+)\alpha}, \end{aligned} \quad (26)$$

where $\langle \omega \rangle_{\text{pair}}$ is the average energy of streaming-neutrinos which annihilate, and the quantities with bar imply those of antineutrinos. The exponential factor in the first line of Eq. (26) is introduced to suppress the heating rate in the optically thick region because the pair-annihilation heating balances with electron-positron pair-annihilation cooling in such a region. G_F is the Fermi coupling constant and $C_{\nu_i \bar{\nu}_i}^{\text{pair}}$ is written by the Weinberg angle θ_W as $C_{\nu_i \bar{\nu}_i}^{\text{pair}} = 1 \pm 4 \sin^2 \theta_W + 8 \sin^4 \theta_W$, where the plus and minus signs denote neutrinos of electron and heavy lepton types, respectively. We use the value $\sin^2 \theta_W \approx 0.2319$. The detailed derivation of Eq. (26) is described in Appendix A.

For our closure relation, $\sqrt{\gamma_{ij} F^i F^j} \approx E$ and $P^{ij} \approx F^i F^j / E$ in the optically thin region. Then the parenthesis of the first line of Eq. (26) becomes

$$(J\bar{J} - 2H^\beta \bar{H}_\beta + L^{\beta\gamma} \bar{L}_{\beta\gamma}) \approx E\bar{E} \left(1 - \frac{F^i \bar{F}_i}{E \bar{E}}\right)^2. \quad (27)$$

Therefore, when the flux vectors of neutrinos and antineutrinos are aligned ($F^i \bar{F}_i \approx E\bar{E}$), the pair-annihilation rate would become very small. This is not physical because, in reality, neutrinos propagate to a variety of directions and thus the pair-annihilation does not vanish even for $\tau_\nu = 0$. For this reason, we may say that the pair-annihilation heating rate is conservatively estimated in our radiation transfer scheme. In Sec. 4.4, we will give a more sophisticated estimation of the pair-annihilation heating rate based on a ray-tracing method.

In order to check the uncertainty in the pair-annihilation heating rate, we perform a simulation in which the pair-annihilation heating rate is calculated assuming the isotropic momentum-space angular distribution for neutrinos. Under this assumption, the pair-annihilation source term $Q_{\text{pair/Iso}, \nu_i}^{(+)}$ ($i = e, x$) is written as

$$Q_{\text{pair/Iso}, \nu_i}^{(+)} = \frac{C_{\nu_i \bar{\nu}_i}^{\text{pair}} G_F^2}{3\pi} \langle \omega \rangle_{\text{pair}} \frac{4}{3} J \bar{J} e^{-\tau_{\nu_i}}. \quad (28)$$

In this model, the pair-annihilation heating rate may be incorporated in an optimistic manner (see Sec. 4.4 for discussion).

For the source terms of Eqs. (11) and (12), we employ the following equations:

$$\mathcal{R}_e = \mathcal{R}_{\text{abs}, \nu_e} - \mathcal{R}_{\text{abs}, \bar{\nu}_e} + \mathcal{R}_{\text{pc}} - \mathcal{R}_{\text{ec}}, \quad (29)$$

$$\mathcal{R}_{\nu_e} = \mathcal{R}_{\text{brems}, \nu_e} + \mathcal{R}_{\text{pair}, \nu_e} + \mathcal{R}_{\text{plasm}, \nu_e} + \mathcal{R}_{\text{ec}}, \quad (30)$$

$$\mathcal{R}_{\bar{\nu}_e} = \mathcal{R}_{\text{brems}, \bar{\nu}_e} + \mathcal{R}_{\text{pair}, \bar{\nu}_e} + \mathcal{R}_{\text{plasm}, \bar{\nu}_e} + \mathcal{R}_{\text{pc}}, \quad (31)$$

$$\mathcal{R}_{\nu_x} = \mathcal{R}_{\text{brems}, \nu_x} + \mathcal{R}_{\text{pair}, \nu_x} + \mathcal{R}_{\text{plasm}, \nu_x}. \quad (32)$$

For these rates except for the electron (anti)neutrino absorption processes, we employ the rates in Fuller et al. (1985), Cooperstein et al. (1986), Ruffert et al. (1996), and Burrows et al. (2006), which are the same as in Sekiguchi et al. (2012).

On the other hand, the source terms due to the electron

(anti)neutrino absorption processes are written as

$$Q_{\text{abs}, \nu_e}^{(+)} \approx \frac{(1 + 3g_A^2) G_F^2}{\pi} \langle \omega_{\nu_e} \rangle_{\text{abs}}^2 (J u^\alpha + H^\alpha) e^{-\tau_{\nu_e}}, \quad (33)$$

$$Q_{\text{abs}, \bar{\nu}_e}^{(+)} \approx \frac{(1 + 3g_A^2) G_F^2}{\pi} \langle \omega_{\bar{\nu}_e} \rangle_{\text{abs}}^2 (\bar{J} u^\alpha + \bar{H}^\alpha) e^{-\tau_{\bar{\nu}_e}}, \quad (34)$$

$$\mathcal{R}_{\text{abs}, \nu_e} \approx \frac{(1 + 3g_A^2) G_F^2}{\pi} \langle \omega_{\nu_e} \rangle_{\text{abs}} J e^{-\tau_{\nu_e}}, \quad (35)$$

$$\mathcal{R}_{\text{abs}, \bar{\nu}_e} \approx \frac{(1 + 3g_A^2) G_F^2}{\pi} \langle \omega_{\bar{\nu}_e} \rangle_{\text{abs}} \bar{J} e^{-\tau_{\bar{\nu}_e}}, \quad (36)$$

where $\langle \omega \rangle_{\text{abs}}$ is the average energy of streaming-neutrinos, and $g_A \approx 1.26$. For the same reason as the pair-annihilation heating, the exponential factors in Eqs. (33)–(36) are introduced in order to suppress these rates in the optically thick region, in which these rates balance with those of their inverse processes. The detailed derivation for these rates are described in Appendix B.

2.4. Initial Condition

We mapped three-dimensional simulation data for a NS-NS merger (Sekiguchi et al. 2015) into two-dimensional data as the initial condition for the axisymmetric neutrino radiation hydrodynamics simulation. Although the merger remnant has a non-axisymmetric structure soon after the onset of the merger, it gradually relaxes into a nearly axisymmetric structure. It also approaches to a quasi-stationary state. In this work, we employ the remnant at about 50 ms after the onset of the merger as an initial condition. In such a phase, the merger remnant is approximately in an axisymmetric quasi-stationary state. We generate axisymmetric data from three-dimensional data by taking average for ρ_* , \hat{e} , \hat{u}_i , Y_e , and Y_{ν_i} as

$$\rho_* = \int \frac{d\varphi}{2\pi} \rho_*^{(3D)}, \quad (37)$$

$$\hat{e} = \frac{1}{\rho_*} \int \frac{d\varphi}{2\pi} \rho_*^{(3D)} \hat{e}^{(3D)}, \quad (38)$$

$$\hat{u}_x = \frac{1}{\rho_*} \int \frac{d\varphi}{2\pi} \rho_*^{(3D)} (+\hat{u}_x^{(3D)} \cos \varphi + \hat{u}_y^{(3D)} \sin \varphi), \quad (39)$$

$$\hat{u}_\varphi = \frac{1}{\rho_*} \int \frac{d\varphi}{2\pi} \rho_*^{(3D)} (-\hat{u}_x^{(3D)} \sin \varphi + \hat{u}_y^{(3D)} \cos \varphi), \quad (40)$$

$$\hat{u}_z = \frac{1}{\rho_*} \int \frac{d\varphi}{2\pi} \rho_*^{(3D)} \hat{u}_z^{(3D)}, \quad (41)$$

$$Y_i = \frac{1}{\rho_*} \int \frac{d\varphi}{2\pi} \rho_*^{(3D)} Y_i^{(3D)}, \quad (42)$$

where the quantities with superscript (3D) imply those taken from the corresponding three-dimensional merger simulation data. After mapping, we re-solve the Hamiltonian and momentum constraint equations assuming the conformally flatness. Employing the conformal flatness may be reasonable because the values of $\tilde{\gamma}_{ij} - \delta_{ij}$ are fairly small or not very large at ~ 50 ms after the merger; specifically the absolute magnitude of all the components is smaller than 0.02.

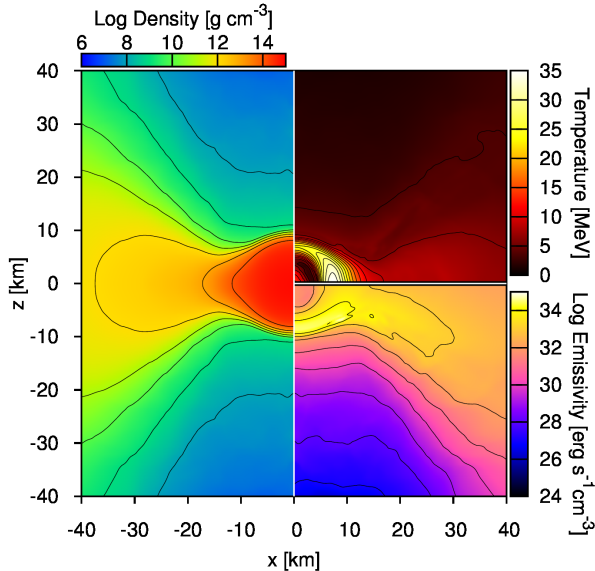


Figure 1. Initial thermodynamical configuration. The rest-mass density (the second and the third quadrant), the temperature (the first quadrant), the flavor-summed effective neutrino emissivity (the fourth quadrant) are shown in the same x - z plane. The black curves denote contours of each quantity. For the temperature, contours are linearly spaced with the interval of 2.5 MeV. For the neutrino emissivity and the rest-mass density, they are logarithmically spaced with the intervals of 1.0 dex.

The configurations of initial thermodynamical quantities are shown in Fig. 1. The MNS is surrounded by a massive torus of mass $\sim 0.2M_{\odot}$. Here we define the mass of the torus as the baryonic mass in the region where the density is lower than $10^{13} \text{ g cm}^{-3}$. The maximum temperature is ~ 30 MeV near the equatorial surface region of the MNS. The temperature of the inner region of the torus is $\sim 5 - 7$ MeV. The effective neutrino emissivity is highest on the polar surface of the MNS and in the inner region of the torus.

We summarize the models for our simulations in Table 1. We refer to the fiducial model as DD2-135135-On-H. In order to understand the effects of the pair-annihilation heating, we also perform a simulation without the neutrino pair-annihilation (the model DD2-135135-Off-H). In addition to these models, we perform a simulation in which the pair-annihilation heating rate is calculated assuming the isotropic momentum-space angular distribution for neutrinos in order to check the uncertainty of the neutrino pair-annihilation heating rate (DD2-135135-Iso-H).

2.5. Grid Setting

We adopt a non-uniform grid in which the grid spacing is increased according to the rule

$$\begin{aligned} \Delta x_{j+1} &= \begin{cases} \Delta x_j & (x_j \leq R_{\text{star}}) \\ (1 + \delta)\Delta x_j & (x_j > R_{\text{star}}), \end{cases} \\ \Delta z_{l+1} &= \begin{cases} \Delta z_l & (z_l \leq R_{\text{star}}) \\ (1 + \delta)\Delta z_l & (z_l > R_{\text{star}}), \end{cases} \end{aligned} \quad (43)$$

where $\Delta x_j \equiv x_{j+1} - x_j$, $\Delta z_l \equiv z_{l+1} - z_l$, δ and R_{star} are constants, and $0 \leq j \leq N$ ($0 \leq l \leq N$). Here, $N + 1$

is the total grid number for one direction. In this grid, a uniform grid with the grid spacing Δx_0 is adopted in the inner region $0 \leq x \leq R_{\text{star}}$ and $0 \leq z \leq R_{\text{star}}$ in order to resolve the MNS. To check the convergence of numerical results, simulations with coarser grid resolutions are also performed (DD2-135135-On-M and DD2-135135-On-L, see Table 1). The values of the innermost grid spacing Δx_0 , the constant δ , the size of the region in which the uniform grid is adopted R_{star} , the grid number N , and the size of computational domain L are also tabulated in Table 1.

3. RESULT

3.1. Dynamics of the System

First, we briefly summarize the dynamics of the fiducial model DD2-135135-On-H. At an early phase of evolution ($t \lesssim 50$ ms), a strong outflow is launched in the vicinity of the rotational axis, which is driven by the neutrino irradiation of dilute matter. The evolution of the rest-mass density, the velocity vector, and the specific heating rate is displayed in the left panel of Fig. 2. This clearly shows that the outflow around the rotational axis is launched. The maximum velocity of the ejecta is $\sim 0.5 c$. We also display snapshots of the rest-mass density, the velocity vector, and the specific heating rate in the absence of the pair-annihilation heating (DD2-135135-Off-H) in the right panel of Fig. 2. For this case, an outflow is launched due to neutrino absorption heating, and the ejecta velocity is much smaller as $0.1 - 0.2 c$. As seen in the right halves of the both panels in Fig. 2, the structure of the specific heating rate is considerably different between the two simulations. The specific heating rate in the polar region of the model DD2-135135-On-H is much higher than that of the model DD2-135135-Off-H because the pair-annihilation heating dominates the other heating processes (i.e., the absorption of electron neutrinos and electron antineutrinos on nuclei). This implies that the high-speed ejecta is launched because of the strong pair-annihilation heating.

At $t \sim 50$ ms, the velocity of the ejecta for the fiducial model decreases to $\sim 0.2 c$ even in the presence of the pair-annihilation heating. This is because the neutrino pair-annihilation heating rate decreases with time as seen in the middle panel of Fig. 2. The decrease of the pair-annihilation heating rate is caused partly by the decrease of the neutrino luminosities. The other reason may attribute to the prescription of the pair-annihilation heating used in our simulation (i.e., Eq. (26)); when a quasi-stationary state is achieved, the flux vectors of neutrinos and antineutrinos are aligned. Then the pair-annihilation heating rate becomes very small as described in Sec. 2.3.2.

3.2. Neutrino Luminosity, Pair-annihilation Rate, and Efficiency

The top panel of Fig. 3 shows the luminosities of individual neutrinos as functions of time. At the beginning of the simulation, the luminosity of electron-type neutrinos is $\sim 10^{53} \text{ erg s}^{-1}$, which is an order of magnitude larger than that of proto-neutron stars formed during the typical supernova explosions (Fischer et al. 2010). In 100 ms, the luminosity decreases rapidly, because the temperature of the torus, which is a strong

Table 1

List of the models. M_{NS} is the gravitational mass of each NS in the merger simulation of Sekiguchi et al. (2015). For Δx_0 , δ , R_{star} , N , and L , see the text in Sec. 2.5.

Model	EOS	M_{NS} (M_{\odot})	Pair-annihilation heating	Δx_0 (m)	δ	R_{star} (km)	N	L (km)
DD2-135135-On-H (fiducial,high)	DD2	1.35	on	150	0.0075	30	951	5440
DD2-135135-Off-H	DD2	1.35	off	150	0.0075	30	951	5440
DD2-135135-Iso-H	DD2	1.35	on, isotropic	150	0.0075	30	951	5440
DD2-135135-On-M (medium)	DD2	1.35	on	200	0.0075	30	871	5790
DD2-135135-On-L (low)	DD2	1.35	on	250	0.0075	30	809	5690

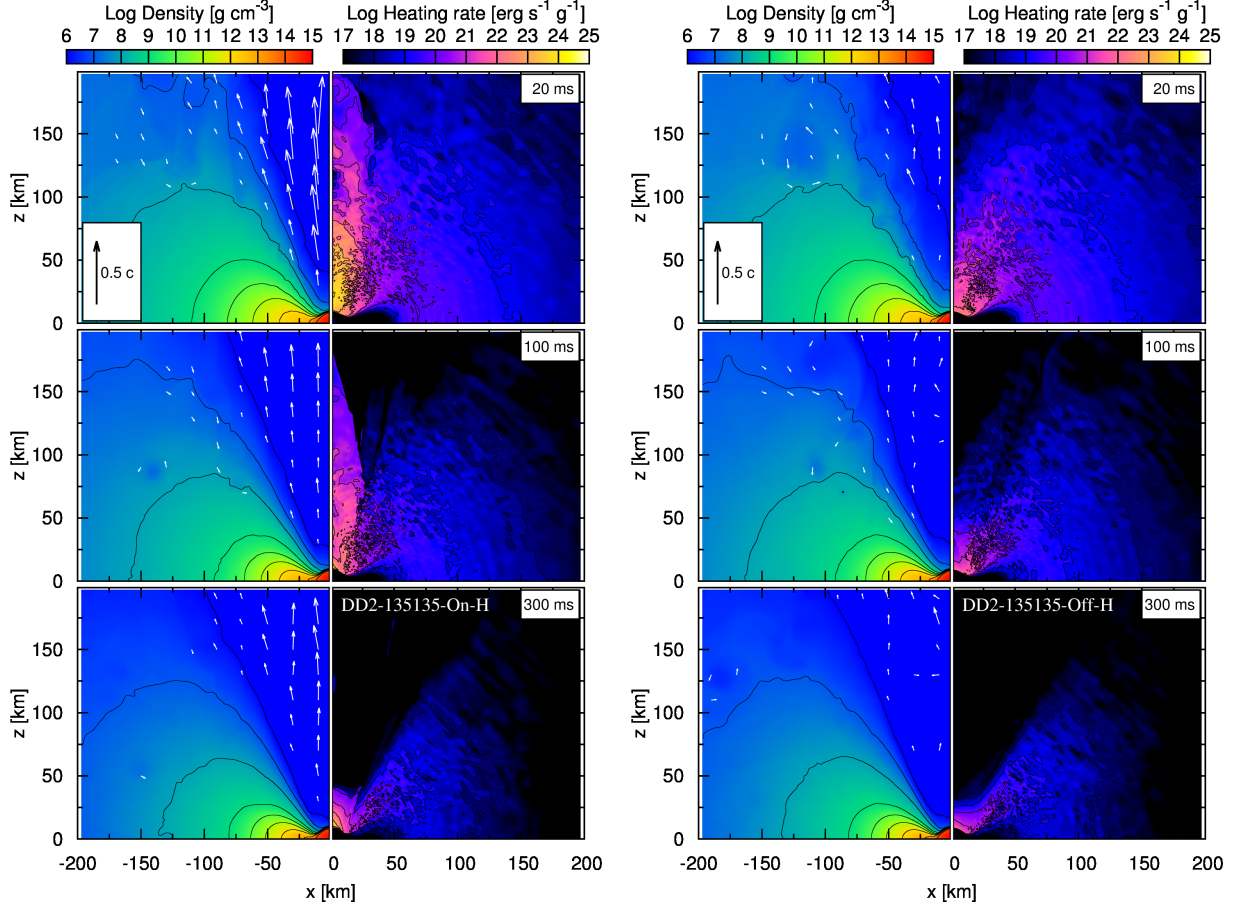


Figure 2. Left: Snapshots of the rest-mass density, the poloidal velocity fields (v^x, v^z), and the specific heating rate for the model DD2-135135-On-H at $t = 20$ ms (top), 100 ms (middle), and 300 ms (bottom) in the meridional plane. The velocity field is plotted only for the case that the velocity is larger than $0.03 c$. Right: Same as the left panel, but for the model DD2-135135-Off-H. For all the figures, the black curves denote logarithmically spaced contours with the intervals of 1.0 dex.

emitter of electron-type neutrinos, decreases (see Fig. 4). For $t \gtrsim 300$ ms, the luminosity settles into nearly constant in time as $\sim 10^{52}$ erg s $^{-1}$. In this phase, a primary source of neutrinos is the MNS and the neutrino emissivity of the torus is much less than that of the MNS.

We define the total pair-annihilation heating rate outside the neutrinosphere as

$$\begin{aligned}
 Q_{\text{pair,tot}} &= \sum_i \int_{\tau_{\nu_i} < 2/3} d\Sigma_\alpha Q_{\text{pair},\nu_i}^{(+)\alpha} \\
 &= \sum_i \int_{\tau_{\nu_i} < 2/3} dx dz 2\pi x W^{-3} w Q_{\text{pair},\nu_i}^{(+)}, \quad (44)
 \end{aligned}$$

where $d\Sigma_\alpha = d^3x \sqrt{\gamma} n_\alpha$ is the three-dimensional volume element on spatial hyper-surfaces. The bottom panel of Fig. 3 shows $Q_{\text{pair,tot}}$ (solid curve) as functions of time. In the fiducial model, $Q_{\text{pair,tot}}$ is $\sim 10^{50}$ erg s $^{-1}$ at $t \sim 50$ ms, and it decreases with time as the neutrino luminosities decrease. For $t \gtrsim 300$ ms, it settles down to $\sim 10^{49}$ erg s $^{-1}$.

In the same figure, we plot the efficiency of the pair-annihilation heating (dashed curves)

$$\eta_{\text{pair}} \equiv \frac{Q_{\text{pair,tot}}}{L_{\nu,\text{tot}}} \quad (45)$$

as a functions of time (Ruffert et al. 1997; Setiawan

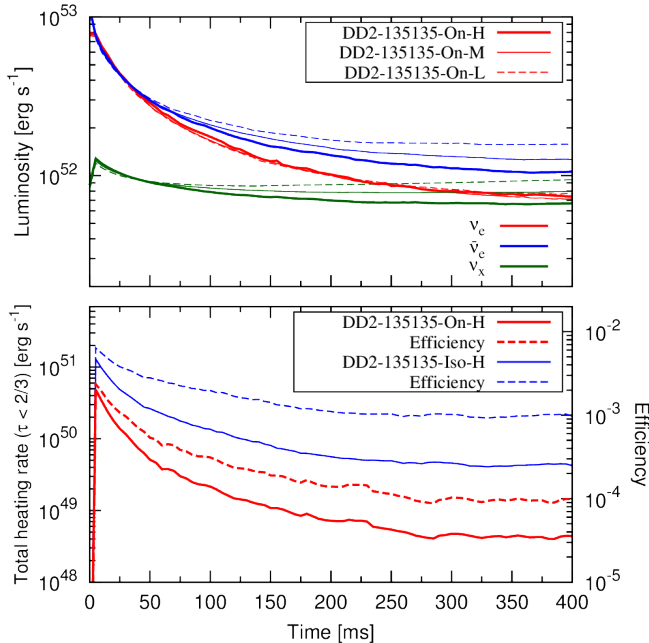


Figure 3. Top: the luminosity of electron neutrinos (red), electron antineutrinos (blue), and other neutrinos (green), respectively. The thick solid, thin solid, and thin dashed curves denote the results for three different resolution models, DD2-135135-On-H (high-resolution), DD2-135135-On-M (medium-resolution) and DD2-135135-On-L (low-resolution), respectively. Bottom: total heating rates due to neutrino pair-annihilation (solid curves) and the heating efficiencies (dashed curves) for the models DD2-135135-On-H (red) and DD2-135135-Iso-H (blue), respectively. The definition for the heating rate is found in Eq. (44).

et al. 2004). Since $Q_{\text{pair,tot}} \propto L_{\nu}^2$, the efficiency is proportional to the neutrino luminosity. Therefore, it decreases with time and eventually settles to $\sim 10^{-4}$ in the quasi-stationary phase. This efficiency is about an order of magnitude lower than those obtained with ray-tracing methods in Ruffert et al. (1997) and Setiawan et al. (2004), and with a Monte-Carlo method in Richers et al. (2015) evaluated with the neutrino luminosities of $\sim 10^{52}$ erg s $^{-1}$. We consider that this is mainly due to the property of M1-scheme that the pair-annihilation is conservatively evaluated as described in Sec. 2.3.2. Our pair-annihilation efficiency is also an order of magnitude lower than that in Just et al. (2016), in which a M1-scheme is employed for the neutrino radiation transport. One of possible reasons would be that they use a multi-energy scheme, in which flux vectors of different energies of neutrinos can cross each other more easily. Hence the problem in M1-scheme might be relaxed. The other reason might be that they take into account viscous heating, which may modify the geometrical and thermal structure of the accretion torus, and the structure of the pair-annihilation heating rate.

3.3. Properties of Neutrino-driven Ejecta

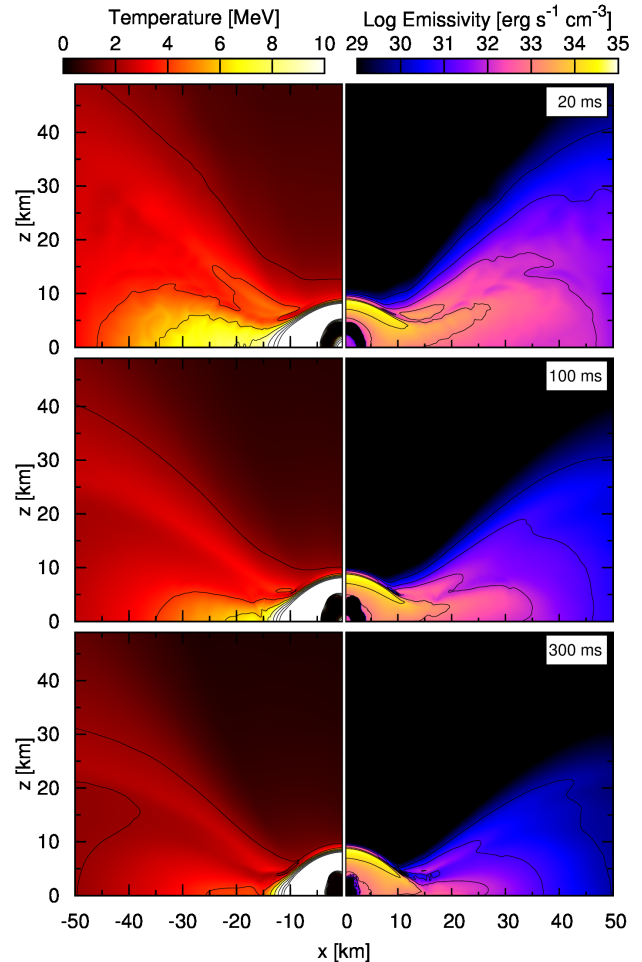


Figure 4. Snapshots of the temperature (left) and the neutrino emission cooling rate (right) for the model DD2-135135-On-H at $t = 20$ ms (top), 100 ms (middle), and 300 ms (bottom) in the meridional plane. The white region in the left panel denotes the region in which the temperature is higher than 10 MeV. The black curves denote contours of each quantity. For the temperature the spacing of the contour is 2.5 MeV. On the other hand, for the cooling rate, the contour is logarithmically spaced with the intervals of 1.0 dex.

We define the baryonic mass, the total energy, and the internal energy of the ejecta as

$$M_{\text{b,ej}} = \int_{|u_t|>1} d\Sigma_{\alpha} \rho u^{\alpha} = \int_{|u_t|>1} dx dz 2\pi x \rho_*, \quad (46)$$

$$E_{\text{tot,ej}} = \int_{|u_t|>1} d\Sigma_{\alpha} \rho \hat{e} u^{\alpha} = \int_{|u_t|>1} dx dz 2\pi x \rho_* \hat{e}, \quad (47)$$

$$E_{\text{int,ej}} = \int_{|u_t|>1} d\Sigma_{\alpha} \rho \varepsilon u^{\alpha} = \int_{|u_t|>1} dx dz 2\pi x \rho_* \varepsilon, \quad (48)$$

where we supposed that fluid elements with $|u_t| > 1$ are gravitationally unbound. Using these values, we define the kinetic energy of the ejecta by

$$E_{\text{kin,ej}} = E_{\text{tot,ej}} - M_{\text{b,ej}} - E_{\text{int,ej}}. \quad (49)$$

We evaluate these values in the cylindrical region of $x \leq 2000$ km and -2000 km $\leq z \leq 2000$ km. We also take into account the mass and energy gone outside this inner region by integrating the fluxes at the boundary of this region and adding them to Eqs. (46)–(48).

We plot the results in Fig. 5. The top panel shows that the ejecta mass increases for the first ~ 100 ms, but the growth rate decreases with time after that. The ejected mass reaches about $8 \times 10^{-4} M_{\odot}$ finally. The kinetic energy, shown in the middle panel, has the same trend as the ejecta mass, and its final value is about 1×10^{49} erg. These values are comparable to those of the dynamical ejecta for the models of the DD2 EOS, which are $\sim 10^{-3} M_{\odot}$ and $\sim 2 \times 10^{49}$ erg (Sekiguchi et al. 2015). Using these quantities, we estimate the averaged velocity of the ejecta V_{ej} by

$$V_{\text{ej}} = \sqrt{\frac{2E_{\text{kin,ej}}}{M_{\text{b,ej}}}}. \quad (50)$$

Note that we do not consider the contribution from a component which was already unbound at the beginning of the simulation, i.e., we only take into account the neutrino-driven ejecta. We show the evolution of V_{ej} in the bottom panel of Fig. 5. The typical velocity of the ejecta is initially about $0.18 c$, but decreases to $0.13 c$ in the quasi-stationary phase. The initial enhancement for V_{ej} is induced by the strong pair-annihilation heating.

In Fig. 5, we also plot the results for the model DD2-135135-Iso-H, in which the pair-annihilation heating rate is taken into account assuming the isotropic angular distribution for neutrinos. The ejecta mass and the kinetic energy for the model DD2-135135-Iso-H are about 1.5 and 4 times larger than those for the fiducial model, respectively. Hence, the averaged velocity of the ejecta for the model DD2-135135-Iso-H is larger as $\sim 0.2 c$ than that in the fiducial model. However, the relativistic outflow is not observed even in this model. The reason would be that the specific heating rate might not be sufficiently high even in this model.

Next, we investigate the mass distributions of the electron fraction and the specific entropy of the ejecta. Figure 6 shows the mass histogram of the ejecta at $t = 300$ ms, at which the amount of the ejecta mass becomes constant in time (see Fig. 5). We find from the left panel that the ejecta are mildly neutron-rich, and have relatively high electron fraction $Y_e > 0.25$, with the typical value ~ 0.4 . This property depends only weakly on the presence of the pair-annihilation heating. This is because the fluid velocity just above the MNS ($z \approx 10$ km) is very small $v \sim 0.01 c$ even in the presence of the pair-annihilation heating (see the top panel of Fig. 7). Hence the neutrino absorption timescale in the polar region, which is estimated using the average energy of the neutrinos $\langle \omega \rangle$ (in $\hbar = 1$ unit) by

$$\begin{aligned} & \frac{4\pi r^2 \langle \omega \rangle}{L_{\nu}} \frac{1}{G_{\text{F}}^2 \langle \omega \rangle^2} \\ & \sim 4 \times 10^{-4} \left(\frac{\langle \omega \rangle}{10 \text{ MeV}} \right)^{-1} \left(\frac{L_{\nu}}{10^{53} \text{ erg/s}} \right)^{-1} \left(\frac{r}{10 \text{ km}} \right)^2 \text{ s}, \end{aligned} \quad (51)$$

is shorter than the time for the fluid element needed to pass the polar region

$$z/v \sim 3 \times 10^{-3} \left(\frac{z}{10 \text{ km}} \right) \left(\frac{v}{0.01c} \right)^{-1} \text{ s}. \quad (52)$$

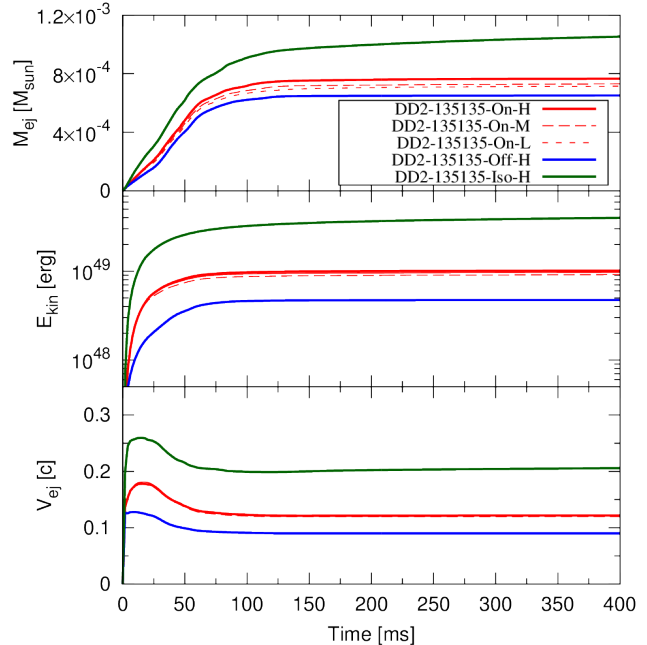


Figure 5. The total mass (top), the total kinetic energy (middle), and the average velocity (bottom) of the ejecta, respectively. The solid red thick curves denote the results for the fiducial model DD2-135135-On-H, and the blue curves denote the result for the model DD2-135135-Off-H, in which the heating process is not taken into account. The thin solid and thin dashed curves denote the result for the low-resolution models DD2-135135-On-M and DD2-135135-On-L, respectively. The green curves denote the results for the model DD2-135135-Iso-H, in which the pair-annihilation heating is calculated assuming the isotropic angular distribution of neutrinos.

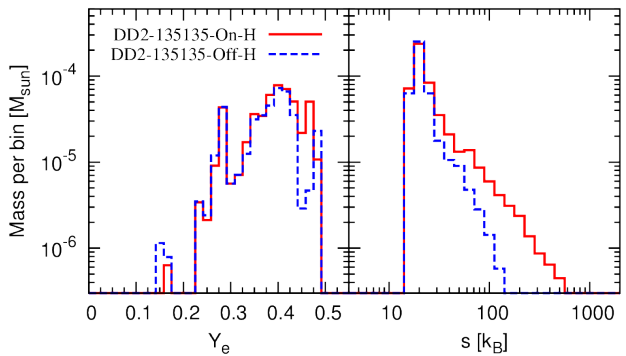


Figure 6. Mass histogram of the neutrino-driven ejecta at $t = 300$ ms. The distributions of the electron fraction (left panel) and the specific entropy (right panel) are shown. The red solid curves denote the results for the fiducial model DD2-135135-On-H, and the blue dashed curves denote the results in the absence of the pair-annihilation heating (i.e., the model DD2-135135-Off-H).

That is, the electron fraction of the ejecta achieves an equilibrium value (e.g., see Eq. (77) in Qian & Woosley 1996) soon after the ejecta is launched from the MNS. From the right panel of Fig. 6, we find that the typical specific entropy of the ejecta is $\sim 10 k_B$. On the other hand, we also find that a small amount of the ejecta has very high specific entropy; the highest value is $500 k_B$. The pair-annihilation heating process generates the high-entropy ejecta because this process heats up the

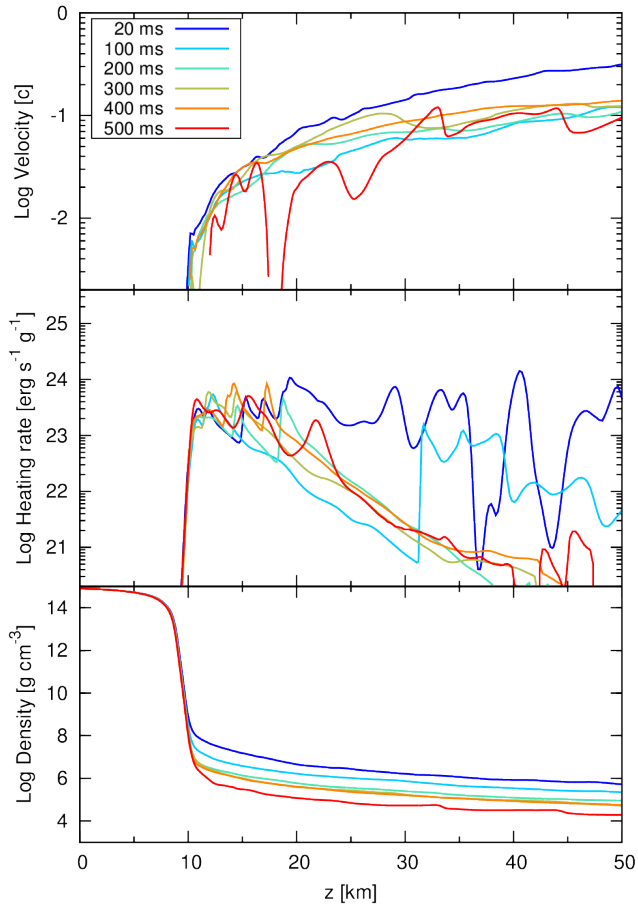


Figure 7. Profiles of the velocity (top), the specific heating rate due to the neutrino pair-annihilation (middle), and the rest-mass density (bottom) along the rotational axis at the timeslices $t=20$, 100, 200, 300, 400, and 500 ms.

material regardless of the baryon density, and hence, a large amount of thermal energy can be injected in the low baryon density region. Implication of these results on the nucleosynthesis is discussed in Sec. 4.2.

3.4. Convergence Test

In Figs. 3 and 5, we plot the results for the lower resolution models DD2-135135-On-M (solid) and DD2-135135-On-L (dashed) by thin curves. For $t \lesssim 100$ ms, the time evolution of the neutrino luminosity depends weakly on the grid resolution. The disagreement in the results among the three different resolution models is $\lesssim 5\%$, so that a convergence is well achieved during this time. On the other hand, the convergence becomes relatively poor for the late time. The difference in the luminosity of electron antineutrinos and heavy-lepton neutrinos between the highest- and lowest-resolution models is $\sim 40\%$ at $t = 400$ ms, while the luminosity of electron neutrinos does not depend on the resolution significantly. The possible reason for this behavior is that the density gradient at the surface of the MNS, which dominates the neutrino emission, becomes steeper at that time, and hence, the diffusion of the neutrino emission is not accurately resolved with the low resolution. We conclude that $L_{\bar{\nu}_e} \lesssim 10^{52}$ erg s $^{-1}$ and $L_{\nu_x} \lesssim 7 \times 10^{51}$ erg s $^{-1}$ at $t = 400$ ms.

For the ejected mass and its kinetic energy (see Fig. 5), the convergence is better achieved. The difference between the highest- and lowest-resolution models is $\sim 3\%$ and $\sim 2\%$ for the mass and the kinetic energy of the ejecta, respectively.

4. DISCUSSION

4.1. Can Neutrinos Drive SGRBs?

As mentioned in Sec. 1, the neutrino pair-annihilation could be a driving force for launching a relativistic ejecta, which could be SGRBs. In the results of our present simulations (DD2-135135-On-H), the kinetic energy of the ejecta ($\sim 10^{49}$ erg) is less than the typical energy (the sum of the energy of gamma-rays in prompt emission and the kinetic energy of the blast wave) of SGRBs of $\sim 10^{50}$ erg (Fong et al. 2015). Moreover, any relativistic outflow is not observed. The primary reason for this is in the presence of high-density baryon in the polar region of the MNS. Even in the model in which the pair-annihilation heating is optimistically evaluated (DD2-135135-Iso-H), the kinetic energy of the ejecta ($\sim 4 \times 10^{49}$ erg) is still lower than $\sim 10^{50}$ erg, and the Lorentz factor of the ejecta is still small ($\Gamma \lesssim 1.3$).

We can estimate the terminal Lorentz factor of the ejecta as

$$\Gamma_f = \frac{Q}{\rho} \tau_{\text{heat}} \approx 1.1 \left(\frac{Q/\rho}{10^{24} \text{ erg g}^{-1} \text{ s}^{-1}} \right) \left(\frac{\tau_{\text{heat}}}{1 \text{ ms}} \right), \quad (53)$$

where Q is the heating rate, and $\tau_{\text{heat}} \sim r/v$ is the heating timescale defined by the length scale of the heating region divided by the fluid velocity of the region. Here, as fiducial values, we take $Q/\rho \sim 10^{24}$ erg g $^{-1}$ s $^{-1}$ and $\tau_{\text{heat}} \sim 30 \text{ km}/0.1 c \approx 1 \text{ ms}$ from the results at $t = 20$ ms shown in Fig. 7. Note that we assume that the internal energy deposited in the material due to heating processes is totally transformed into the kinetic energy. The small Lorentz factor in our simulation ($\Gamma \lesssim 1.3$) is consistent with the estimate of Eq. (53).

In order to obtain the Lorentz factor of ~ 100 , the specific heating rate needs to be $Q/\rho \sim 10^{26}$ erg g $^{-1}$ s $^{-1}$ over a length scale of ~ 30 km. We plot the density structure along the rotational axis in the bottom panel of Fig. 7. This shows that the density decreases with time gradually, so that the heating rate required to achieve the outflow with high Lorentz factor also decreases with time. For example, for $t \gtrsim 400$ ms, the density decreases to $\lesssim 10^5$ g cm $^{-3}$. Then the heating rate required to launch the ultra-relativistic ejecta is $Q \sim 10^{31}$ erg cm $^{-3}$ s $^{-1}$. Such a high heating rate is indeed achieved in the first ~ 10 ms in our simulation (see Fig. 8), at which the system has very large neutrino luminosity of $\sim 10^{53}$ erg s $^{-1}$. Therefore, the relativistic outflow could be launched for later times if such a high luminosity is sustained.

4.2. Nucleosynthesis in the Neutrino-driven Ejecta

Most of the neutrino-driven ejecta has the electron fraction between 0.3 and 0.5 and the specific entropy $\sim 10 - 20 k_B$. Therefore, the strong r -process may not occur in this type of the ejecta (Hoffman et al. 1997; Martin et al. 2015). Moreover, since the amount of the mass of the neutrino-driven ejecta is small, this component would play a minor role for the entire nucleosyn-

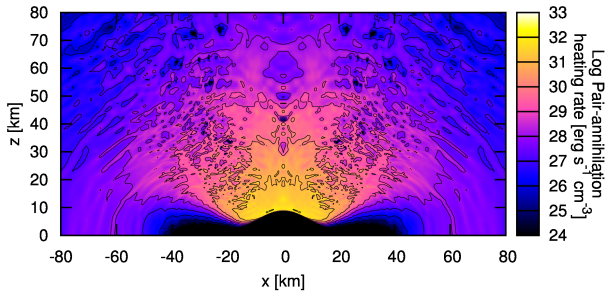


Figure 8. Snapshot of the neutrino pair-annihilation heating rate for the fiducial model DD2-135135-On-H at $t = 10$ ms in the meridional plane. The black curves denote logarithmically spaced contours with the intervals of 1.0 dex.

thesis. On the other hand, due to the effect of the pair-annihilation heating, a small amount of very high specific entropy material of $s \sim 500 k_B$ is ejected (see Fig. 6). The electron fraction of such a ejecta is $\sim 0.45 - 0.50$, and the expansion velocity is $\sim 0.2 - 0.5 c$.

In such a high-entropy and fast-expanding material, heavy nuclei could be synthesized through the r -process (the condition for the r -process nucleosynthesis is found, e.g. see Hoffman et al. 1997). Even in a slightly proton-rich condition, if the entropy and expansion velocity of the ejecta are sufficiently high, a lot of alpha particles and nucleons remain in low-temperature environment due to alpha-rich freeze-out. Then the heavy nuclei could be produced through the nucleon capture process as described in Meyer (2002) and Fujibayashi et al. (2016). To explore these issues, we need a detailed nucleosynthesis calculation.

4.3. Effects of the Viscosity

In our simulations, the viscous effect, which is likely to be induced by the magnetohydrodynamical turbulent motion (Balbus & Hawley 1998; Hawley et al. 2013; Suzuki & Inutsuka 2014; Salvesen et al. 2016; Shi et al. 2016) is not taken into account. Recent general relativistic magnetohydrodynamics simulations for NS-NS mergers suggest that strongly magnetized MNS and torus are formed after the merger via the Kelvin-Helmholtz and the magnetorotational instabilities (Kiuchi et al. 2014, 2015a). The turbulent flow in the torus is sustained by the magnetorotational instability and the flow transports the angular momentum. Moreover, the dissipation of the turbulent motion heats up the torus. The dynamics of the system could be changed significantly by the effective viscosity.

First, the properties of the torus could be modified. For example, the geometrical thickness of the torus could be enhanced due to the viscous heating, and in addition, the torus could spread outward due to the angular momentum transport (Shibata et al. in submission). Furthermore, the viscous heating could rise the temperature inside the torus, and as a result, the neutrino luminosity of the torus would be increased. Then the heating due to neutrinos would be enhanced and will help driving a relativistic jet from the polar region of MNS as discussed in Sec. 4.1.

Second, in addition to the neutrino-driven wind, the

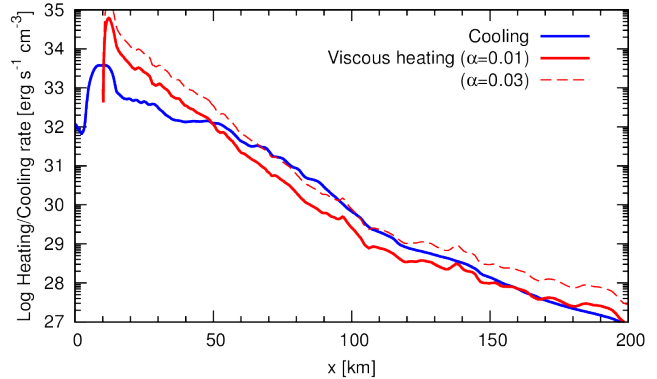


Figure 9. Viscous heating rates (red curves) and neutrino emission cooling rate (blue curve). For the viscous heating rates, we assume $\alpha = 0.01$ for solid curve and $\alpha = 0.03$ for dashed curve.

viscosity-driven wind from the torus is expected. As suggested in the previous works (Fernández & Metzger 2013; Metzger & Fernández 2014; Fernández et al. 2015; Kiuchi et al. 2015b), $\sim 10\%$ of the torus mass may be ejected as the viscosity-driven wind, so that the properties of the mass ejection in the viscous time scale ~ 100 ms would be affected by the viscous effect. We plan to perform viscous radiation hydrodynamics simulations in our next work.

We can roughly estimate the viscous effects using a snapshot of the present non-viscous simulations. In an axisymmetric, geometrically thin, and stationary accretion disk, the viscous heating rate $Q_{\text{vis}}^{(+)}$ becomes

$$Q_{\text{vis}}^{(+)} = \rho\nu \left(x \frac{\partial\Omega}{\partial x} \right)^2, \quad (54)$$

where we employed a Shakura-Sunyaev parametrization of the kinetic viscosity coefficient (Shakura & Sunyaev 1973; Kato et al. 2008) as

$$\nu = \alpha \frac{c_s^2}{\Omega} = \alpha \frac{c_s^2 x}{v_\phi} \quad (55)$$

We show the viscous heating rate and neutrino emission cooling rate ($\sum_i Q_{(\text{leak})\nu_i}$) on the equatorial plane as functions of the radius in Fig. 9. Here we used the axisymmetric configuration at the beginning of the simulation. We assumed $\alpha \sim 10^{-2}$ as a fiducial value following the latest results by high-resolution magnetohydrodynamics simulation (Hawley et al. 2013; Suzuki & Inutsuka 2014; Salvesen et al. 2016; Shi et al. 2016). We find that the viscous heating rate is comparable to the cooling rate. This suggests that, due to the viscous heating, the energy loss by the neutrino cooling may be compensated, and the temperature of the torus would decrease slower than that in the simulation without the viscosity. Therefore, in reality, the initially large neutrino luminosity would be sustained for a longer timescale and the mass and the kinetic energy of the neutrino-driven ejecta would be larger in the presence of the viscous effect.

4.4. Pair-annihilation Heating Rate Calculated with the Ray-tracing Method

It is known that the M1-closure scheme has a problem in the optically thin region (e.g., Jiang et al. 2014;

Ohsuga & Takahashi 2016; Takahashi et al. 2016; Frank et al. 2006). As a result, the pair-annihilation heating rate evaluated in our present work can be significantly different from more realistic one. This is recognized from the fact that the cross section of the pair-annihilation process has strong angle-dependence ($\propto (1 - \cos \Theta)^2$ with

Θ being the scattering angle between two neutrinos).

Here we estimate the heating rates in terms of the ray-tracing method (Ruffert et al. 1997; Zalamea & Beloborodov 2011) using each snapshot of the simulation. According to Ruffert et al. (1997), the heating rate due to the pair-annihilation in this scheme can be written (in $\hbar = 1$ unit) as

$$Q_{\text{pair}, \nu_i}^{(+)} = \frac{C_{\nu_i \bar{\nu}_i}^{\text{pair}} G_F^2}{3\pi} \int dV_1 \int dV_2 \langle \omega \rangle_{\text{pair}} Q_{(\text{leak}) \nu_i}^{(-)}(x_1) Q_{(\text{leak}) \bar{\nu}_i}^{(-)}(x_2) \frac{(1 - \cos \Theta)^2}{\pi^2 |x - x_1| |x - x_2|}, \quad (56)$$

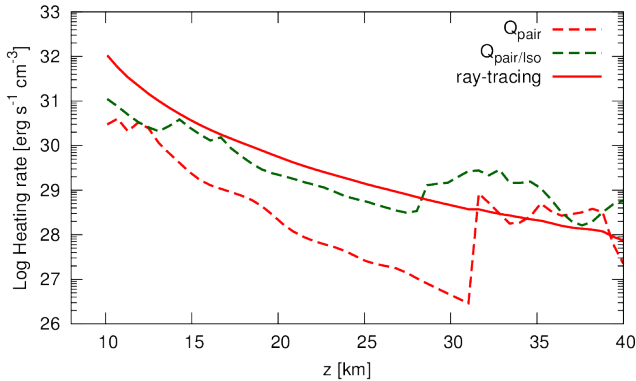


Figure 10. Neutrino pair-annihilation heating rate along the rotational axis at $t = 100$ ms. The red solid curve denotes the heating rate calculated with a ray-tracing method. The red and green dashed curves denote the heating rates for the models DD2-135135-On-H and DD2-135135-Iso-H, respectively.

where $dV = d^3x \sqrt{\gamma}$ is the physical volume element, $\cos \Theta = (x - x_1) \cdot (x - x_2) / |x - x_1| |x - x_2|$ is the angle between the momenta of colliding neutrinos, and $Q_{(\text{leak}) \nu_i}^{(-)}$ is the leakage source term for neutrinos of the flavor i except for the heating processes. Here we do not consider the general relativistic effects such as the bending of neutrino trajectories and gravitational redshift. For the average energy of neutrinos $\langle \omega \rangle_{\text{pair}}$, we employ the value used in the radiation hydrodynamics simulation (see Eq. (A11)) in order to focus only on the difference in the scattering angle.

We show the pair-annihilation heating rate using the ray-tracing method along the rotational (z -) axis in Fig. 10. It is found that the heating rate based on the moment-formalism is underestimated by factor of $\gtrsim 10$ compared with the results in the ray-tracing framework. Moreover, the average energy of neutrinos which annihilate, $\langle \omega \rangle_{\text{pair}}$, employed in our simulation might be smaller than the real one as described in Appendix A. To conclude, the pair-annihilation heating rate employed in our simulation might be at least 10 times underestimated.

On the other hand, the pair-annihilation heating rate based on the assumption of isotropic angular distribution of neutrinos could provide a result that agrees with that in the ray-tracing framework in a better manner than that in the moment-formalism for the region shown in Fig. 10. This is because, near the MNS, neutrinos prop-

agate in various directions due to the neutrino emission from the torus and the MNS. This suggests that, for the region at which the pair-annihilation heating is efficient, we need to take into account the angular distribution of neutrinos more carefully.

5. SUMMARY

We performed a fully general relativistic, axisymmetric numerical relativity simulation for a MNS surrounded by a torus, which is the typical remnant of the NS-NS merger. We took into account neutrino transport using the truncated moment formalism with M1-closure and relevant weak interaction reactions between neutrinos and the fluid material including the neutrino pair-annihilation in an approximate manner. For the initial condition of this simulation, we used a configuration obtained in a three-dimensional, numerical relativity simulation for the NS-NS merger. Our purpose is to investigate the amount and the properties of the material ejected due to the neutrino heating in the framework of purely radiation-hydrodynamics simulation.

In this setup, a quasi-stationary neutrino-driven outflow is launched for ~ 300 ms from the beginning of the simulation. The effect of the neutrino pair-annihilation heating is quite large because of the very high neutrino luminosity of the MNS and the torus. Furthermore, due to the existence of the dense and hot torus, the structure of the heating rate density is quite different from the isolated NS usually considered as normal core-collapse supernova remnants. For the DD2 EOS, the mass and the kinetic energy of the neutrino-driven ejecta are comparable to those of the dynamical ejecta (Sekiguchi et al. 2015). Therefore, the neutrino-driven ejecta would contribute to the mass and kinetic energy of the entire ejecta of the NS-NS merger for this EOS.

An interesting finding is that, due to the neutrino pair-annihilation heating, a small amount of the ejected material has a very high specific entropy $\sim 500 k_B$ and the velocity of the ejecta is $\sim 0.5 c$. Such high specific entropy is not achieved for the neutrino-driven winds in the normal supernovae and other astrophysical phenomena, so that a unique nucleosynthesis process could proceed in the ejecta.

The relativistic outflow required for SGRBs is not found in our present simulation because the specific heating rate around the rotational axis is small. The reasons for this might be the small pair-annihilation heating rate and the baryon pollution due to the neutrino-driven wind

from the MNS. Moreover, the kinetic energy of the ejecta is less than the typical value of the SGRBs. Our results suggest that, in this purely-radiation hydrodynamics case, the neutrino pair-annihilation process in MNS-torus system cannot account for the majority of observed SGRB events. However, we used an approximate neutrino transport scheme at this point, and hence the final conclusion should be drawn by performing simulations fully solving Boltzmann's equation for neutrino transport. Moreover, we do not consider the effects of magnetohydrodynamic turbulence in our simulations. Hence the neutrino emissivity could be underestimated because the viscous heating associated with the turbulence motion would enhance the neutrino luminosity. For this reason, in the future, we plan to perform more sophisticated simulations considering these missing elements.

In order to obtain the relativistic outflow from this MNS-torus system, the high neutrino luminosity of $\sim 10^{53}$ erg s $^{-1}$ would be needed at later time, for which the density in the polar region decreases to $\lesssim 10^5$ g cm $^{-3}$. Such a high neutrino luminosity may be achieved due to the viscous heating in the accretion torus.

S. F. thanks Takahiro Tanaka, Kunihito Ioka, and Yudai Suwa for fruitful discussions. S. F. also thanks Kohsuke Sumiyoshi for discussions about the radiation transfer and the emission processes of neutrinos. This work was initiated during S.F.'s stay in Toho University, and S. F. thanks Tetsu Kitayama for willingly accepting S.F.'s visit to the university. S. F. is supported by Research Fellowship of Japan Society for the Promotion of Science (JSPS) for Young Scientists (No.26-1329). This work was supported by JSPS Grant-in-Aid for Scientific Research (16H02183, 15H00836, 15K05077, 15H00783, 16K17706, 16H06341, 15H00782), by the HPCI Strategic Program of Japanese MEXT, and by a MEXT program "Priority Issue 9 to be tackled by using Post K computer". Numerical simulations were carried out on Cray XC40 in Yukawa Institute for Theoretical Physics, Kyoto University and FX10 in Information Technology Center, the University of Tokyo. Numerical analyses were carried out on computers at Center for Computational Astrophysics, National Astronomical Observatory of Japan.

REFERENCES

- Abadie, J., et al. 2010, *Nuclear Instruments and Methods in Physics Research A*, 624, 223
- Accadia, T., et al. 2011, *Classical and Quantum Gravity*, 28, 114002
- Alcubierre, M., Brügmann, B., Diener, P., Koppitz, M., Pollney, D., Seidel, E., & Takahashi, R. 2003, *Phys. Rev. D*, 67, 084023
- Alcubierre, M., Brügmann, B., Holz, D., Takahashi, R., Brandt, S., Seidel, E., Thornburg, J., & Ashtekar, A. 2001, *International Journal of Modern Physics D*, 10, 273
- Antoniadis, J., et al. 2013, *Science*, 340, 448
- Balbus, S. A., & Hawley, J. F. 1998, *Reviews of Modern Physics*, 70, 1
- Banik, S., Hempel, M., & Bandyopadhyay, D. 2014, *ApJS*, 214, 22
- Baumgarte, T. W., & Shapiro, S. L. 1999, *Phys. Rev. D*, 59, 024007
- Blandford, R. D., & Znajek, R. L. 1977, *MNRAS*, 179, 433
- Brügmann, B., González, J. A., Hannam, M., Husa, S., Sperhake, U., & Tichy, W. 2008, *Phys. Rev. D*, 77, 024027
- Burrows, A., Reddy, S., & Thompson, T. A. 2006, *Nuclear Physics A*, 777, 356
- Campanelli, M., Lousto, C. O., Marronetti, P., & Zlochower, Y. 2006, *Physical Review Letters*, 96, 111101
- Cooperstein, J. 1988, *Phys. Rep.*, 163, 95
- Cooperstein, J., van den Horn, L. J., & Baron, E. A. 1986, *ApJ*, 309, 653
- Demorest, P. B., Pennucci, T., Ransom, S. M., Roberts, M. S. E., & Hessels, J. W. T. 2010, *Natur*, 467, 1081
- Dessart, L., Ott, C. D., Burrows, A., Rosswog, S., & Livne, E. 2009, *ApJ*, 690, 1681
- Dietrich, T., Bernuzzi, S., Ujevic, M., & Brügmann, B. 2015, *Phys. Rev. D*, 91, 124041
- Eichler, D., Livio, M., Piran, T., & Schramm, D. N. 1989, *Natur*, 340, 126
- Fernandez, N., et al. 2013, *Physical Review Letters*, 111, 108301
- Fernández, R., Kasen, D., Metzger, B. D., & Quataert, E. 2015, *MNRAS*, 446, 750
- Fernández, R., & Metzger, B. D. 2013, *MNRAS*, 435, 502
- Fischer, T., Whitehouse, S. C., Mezzacappa, A., Thielemann, F.-K., & Liebendörfer, M. 2010, *A&A*, 517, A80
- Fong, W., Berger, E., Margutti, R., & Zauderer, B. A. 2015, *ApJ*, 815, 102
- Foucart, F., et al. 2016, *Phys. Rev. D*, 93, 044019
- Frank, M., Dubroca, B., & Klar, A. 2006, *Journal of Computational Physics*, 218, 1
- Freiburghaus, C., Rosswog, S., & Thielemann, F.-K. 1999, *ApJL*, 525, L121
- Fujibayashi, S., Yoshida, T., & Sekiguchi, Y. 2016, *ApJ*, 818, 96
- Fuller, G. M., Fowler, W. A., & Newman, M. J. 1985, *ApJ*, 293, 1
- González, M., Audit, E., & Huynh, P. 2007, *A&A*, 464, 429
- Goriely, S., Bauswein, A., & Janka, H.-T. 2011, *ApJL*, 738, L32
- Hawley, J. F., Richers, S. A., Guan, X., & Krolik, J. H. 2013, *ApJ*, 772, 102
- Hempel, M., Fischer, T., Schaffner-Bielich, J., & Liebendörfer, M. 2012, *ApJ*, 748, 70
- Hoffman, R. D., Woosley, S. E., & Qian, Y.-Z. 1997, *ApJ*, 482, 951
- Hotokezaka, K., Kiuchi, K., Kyutoku, K., Muranushi, T., Sekiguchi, Y.-i., Shibata, M., & Taniguchi, K. 2013, *Phys. Rev. D*, 88, 044026
- Hotokezaka, K., Kyutoku, K., Okawa, H., Shibata, M., & Kiuchi, K. 2011, *Phys. Rev. D*, 83, 124008
- Jiang, Y.-F., Stone, J. M., & Davis, S. W. 2014, *ApJS*, 213, 7
- Just, O., Obergaulinger, M., Janka, H.-T., Bauswein, A., & Schwarz, N. 2016, *ApJL*, 816, L30
- Kaplan, J. D., Ott, C. D., O'Connor, E. P., Kiuchi, K., Roberts, L., & Duez, M. 2014, *ApJ*, 790, 19
- Kasen, D., Badnell, N. R., & Barnes, J. 2013, *ApJ*, 774, 25
- Kato, S., Fukue, J., & Mineshige, S. 2008, *Black-Hole Accretion Disks — Towards a New Paradigm —* (Kyoto University Press)
- Kiuchi, K., Cerdá-Durán, P., Kyutoku, K., Sekiguchi, Y., & Shibata, M. 2015a, *Phys. Rev. D*, 92, 124034
- Kiuchi, K., Kyutoku, K., Sekiguchi, Y., Shibata, M., & Wada, T. 2014, *Phys. Rev. D*, 90, 041502
- Kiuchi, K., Sekiguchi, Y., Kyutoku, K., Shibata, M., Taniguchi, K., & Wada, T. 2015b, *Phys. Rev. D*, 92, 064034
- Kiuchi, K., Sekiguchi, Y., Shibata, M., & Taniguchi, K. 2009, *Phys. Rev. D*, 80, 064037
- , 2010, *Physical Review Letters*, 104, 141101
- Kuroda, K., & LCGT Collaboration. 2010, *Classical and Quantum Gravity*, 27, 084004
- Lattimer, J. M., & Schramm, D. N. 1974, *ApJL*, 192, L145
- Levermore, C. D. 1984, *J. Quant. Spectrosc. Radiat. Transfer*, 31, 149
- Li, L.-X., & Paczyński, B. 1998, *ApJL*, 507, L59
- Marronetti, P., Tichy, W., Brügmann, B., González, J., & Sperhake, U. 2008, *Phys. Rev. D*, 77, 064010
- Martin, D., Perego, A., Arcones, A., Thielemann, F.-K., Korobkin, O., & Rosswog, S. 2015, *ApJ*, 813, 2
- Meszaros, P., & Rees, M. J. 1992, *MNRAS*, 257, 29P
- Metzger, B. D., & Fernández, R. 2014, *MNRAS*, 441, 3444
- Meyer, B. S. 2002, *Physical Review Letters*, 89, 231101
- Narayan, R., Paczynski, B., & Piran, T. 1992, *ApJL*, 395, L83
- Ohsuga, K., & Takahashi, H. R. 2016, *ApJ*, 818, 162
- Perego, A., Rosswog, S., Cabezón, R. M., Korobkin, O., Käppeli, R., Arcones, A., & Liebendörfer, M. 2014, *MNRAS*, 443, 3134
- Perego, A., Yasin, H., & Arcones, A. 2017, *ArXiv e-prints*
- Qian, Y.-Z., & Woosley, S. E. 1996, *ApJ*, 471, 331
- Richers, S., Kasen, D., O'Connor, E., Fernández, R., & Ott, C. D. 2015, *ApJ*, 813, 38

- Rosswog, S., Liebendörfer, M., Thielemann, F.-K., Davies, M. B., Benz, W., & Piran, T. 1999, *A&A*, 341, 499
- Ruffert, M., Janka, H.-T., & Schaefer, G. 1996, *A&A*, 311, 532
- Ruffert, M., Janka, H.-T., Takahashi, K., & Schaefer, G. 1997, *A&A*, 319, 122
- Salmonson, J. D., & Wilson, J. R. 1999, *ApJ*, 517, 859
- Salvesen, G., Simon, J. B., Armitage, P. J., & Begelman, M. C. 2016, *MNRAS*, 457, 857
- Sekiguchi, Y. 2010, *Progress of Theoretical Physics*, 124, 331
- Sekiguchi, Y., Kiuchi, K., Kyutoku, K., & Shibata, M. 2011, *Physical Review Letters*, 107, 051102
- . 2012, *Progress of Theoretical and Experimental Physics*, 2012, 01A304
- . 2015, *Phys. Rev. D*, 91, 064059
- Sekiguchi, Y., Kiuchi, K., Kyutoku, K., Shibata, M., & Taniguchi, K. 2016, *Phys. Rev. D*, 93, 124046
- Setiawan, S., Ruffert, M., & Janka, H.-T. 2004, *MNRAS*, 352, 753
- Shakura, N. I., & Sunyaev, R. A. 1973, *A&A*, 24, 337
- Shi, J.-M., Stone, J. M., & Huang, C. X. 2016, *MNRAS*, 456, 2273
- Shibata, M. 2003a, *Phys. Rev. D*, 67, 024033
- . 2003b, *ApJ*, 595, 992
- Shibata, M., Kiuchi, K., & Sekiguchi, Y. in submission, *Phys. Rev. D*
- Shibata, M., Kiuchi, K., Sekiguchi, Y., & Suwa, Y. 2011, *Progress of Theoretical Physics*, 125, 1255
- Shibata, M., & Nakamura, T. 1995, *Phys. Rev. D*, 52, 5428
- Shibata, M., & Taniguchi, K. 2006, *Phys. Rev. D*, 73, 064027
- Shibata, M., Taniguchi, K., & Uryū, K. 2005, *Phys. Rev. D*, 71, 084021
- Suzuki, T. K., & Inutsuka, S.-i. 2014, *ApJ*, 784, 121
- Symbalisty, E., & Schramm, D. N. 1982, *Astrophys. Lett.*, 22, 143
- Takahashi, H. R., Ohsuga, K., Kawashima, T., & Sekiguchi, Y. 2016, *ApJ*, 826, 23
- Takami, K., Rezzolla, L., & Baiotti, L. 2015, *Phys. Rev. D*, 91, 064001
- Tanaka, M., & Hotokezaka, K. 2013, *ApJ*, 775, 113
- Thorne, K. S. 1981, *MNRAS*, 194, 439
- Timmes, F. X., & Swesty, F. D. 2000, *ApJS*, 126, 501
- Usov, V. V. 1992, *Natur*, 357, 472
- Wanajo, S., Sekiguchi, Y., Nishimura, N., Kiuchi, K., Kyutoku, K., & Shibata, M. 2014, *ApJL*, 789, L39
- Zalamea, I., & Beloborodov, A. M. 2011, *MNRAS*, 410, 2302

APPENDIX

PRESCRIPTION OF NEUTRINO-ANTINEUTRINO PAIR-ANNIHILATION HEATING RATE IN ENERGY-INTEGRATED M1-SCHEME

In the fluid rest frame, the energy deposition rate for a neutrino species ν_i due to the pair-annihilation process is written (in $\hbar = 1$ unit) as

$$Q_{\text{pair},\nu_i}^{(+)} = \int \frac{d^3k}{(2\pi)^3} \int \frac{d^3k'}{(2\pi)^3} \omega f_{\nu_i}(k) f_{\bar{\nu}_i}(k') \sigma_{\text{pair},i}(k, k'), \quad (\text{A1})$$

where $f_{\nu_i}(k)$ and $f_{\bar{\nu}_i}(k')$ are the distribution functions of the i -th species of neutrinos and antineutrinos, which are functions of momenta k and k' , respectively, and $\omega = -u^\alpha k_\alpha$ is the energy of neutrinos in the fluid rest frame. The cross section of the pair-annihilation process ($\nu_i + \bar{\nu}_i \rightarrow e^- + e^+$), $\sigma_{\text{pair},i}(k, k')$, is written (see, e.g., Salmonson & Wilson 1999) as

$$\sigma_{\text{pair},i}(k, k') \approx \frac{C_{\nu_i\bar{\nu}_i}^{\text{pair}} G_{\text{F}}^2 (k \cdot k')^2}{3\pi \omega \omega'} = \frac{C_{\nu_i\bar{\nu}_i}^{\text{pair}} G_{\text{F}}^2}{3\pi} \omega \omega' (1 - \ell^\alpha \ell'_\alpha)^2, \quad (\text{A2})$$

where we ignored the phase space blocking for electrons and positrons, and the electron mass (≈ 0.511 MeV) because the energy of neutrinos (~ 10 MeV) is much higher. Here we defined a spatial unit four-vector ℓ^α orthogonal to u^α as

$$k^\alpha = \omega(u^\alpha + \ell^\alpha). \quad (\text{A3})$$

In our moment formalism (Shibata et al. 2011), we define the energy-integrated zeroth-, first-, and second-rank moments of neutrinos by

$$J = \int d\omega d\Omega \left(\frac{\omega}{2\pi}\right)^3 f(k), \quad (\text{A4})$$

$$H^\alpha = \int d\omega d\Omega \left(\frac{\omega}{2\pi}\right)^3 f(k) \ell^\alpha, \quad (\text{A5})$$

$$L^{\alpha\beta} = \int d\omega d\Omega \left(\frac{\omega}{2\pi}\right)^3 f(k) \ell^\alpha \ell^\beta, \quad (\text{A6})$$

where the solid angle Ω is the direction of the momentum of neutrinos in the fluid rest frame. In order to evaluate the heating rate using the above moments, we approximate the energy of neutrinos, ω , by its average value $\langle \omega \rangle_{\text{pair}}$. Then Eq. (A1) becomes

$$\begin{aligned} Q_{\text{pair},\nu_i}^{(+)} &\approx \langle \omega \rangle_{\text{pair}} \frac{C_{\nu_i\bar{\nu}_i}^{\text{pair}} G_{\text{F}}^2}{3\pi} \int d\omega d\Omega \left(\frac{\omega}{2\pi}\right)^3 \int d\omega' d\Omega' \left(\frac{\omega'}{2\pi}\right)^3 f_{\nu_i}(k) f_{\bar{\nu}_i}(k') (1 - \ell^\alpha \ell'_\alpha)^2 \\ &= \frac{C_{\nu_i\bar{\nu}_i}^{\text{pair}} G_{\text{F}}^2}{3\pi} \langle \omega \rangle_{\text{pair}} (J\bar{J} - 2H^\beta \bar{H}_\beta + L^{\beta\gamma} \bar{L}_{\beta\gamma}), \end{aligned} \quad (\text{A7})$$

which appeared in Eq. (26).

In order to evaluate the average energy of streaming-neutrinos $\langle\omega\rangle_{\text{pair}}$ in our energy-integrated radiation transfer scheme, we assume that streaming-neutrinos have the Fermi-Dirac-type energy distribution, i.e.,

$$f_\nu(\omega) = \frac{1}{e^{\omega/T_\nu - \eta_\nu} + 1}. \quad (\text{A8})$$

Then the energy density of neutrinos in the fluid rest frame J , the “temperature” of the neutrino T_ν , and the normalized “chemical potential” of streaming-neutrinos η_ν satisfy the relation

$$J = \int d\omega \frac{\omega^3}{(2\pi)^3} \frac{1}{e^{\omega/T_\nu - \eta_\nu} + 1} = \frac{T_\nu^4}{(2\pi)^3} F_3(\eta_\nu), \quad (\text{A9})$$

where $F_k(\eta)$ is the relativistic Fermi integral of order k defined by

$$F_k(\eta) = \int dx \frac{x^k}{e^{x-\eta} + 1}. \quad (\text{A10})$$

We assumed that the “temperature” of streaming-neutrinos T_ν is the same as the local temperature of the matter T . Then we obtain the normalized “chemical potential” of neutrinos, η_ν , by solving Eq. (A9). The average energy of streaming-neutrinos is then evaluated as

$$\langle\omega\rangle_{\text{pair}} = \frac{F_4(\eta_\nu)}{F_3(\eta_\nu)} T. \quad (\text{A11})$$

This average energy would be smaller than the real one because the temperature of neutrinos is comparable to the temperature of their emission region, which is usually higher than that of the free-streaming region of neutrinos. For this reason, we should keep in mind that the pair-annihilation heating rate would be evaluated by our scheme in a conservative manner.

PRESCRIPTION OF NEUTRINO ABSORPTION PROCESSES IN ENERGY-INTEGRATED M1-SCHEME

In the same way as Eq. (A1), the source terms due to the absorption of electron (anti)neutrinos are written (in $\hbar = 1$ unit) as

$$\begin{aligned} Q_{\text{abs},\nu_e/\bar{\nu}_e}^{(+)\alpha} &= \int \frac{d^3k}{(2\pi)^3} k^\alpha f_{\nu_e/\bar{\nu}_e}(k) \sigma_{\text{abs},\nu_e/\bar{\nu}_e}(k) \\ &= \int d\omega d\Omega \left(\frac{\omega}{2\pi}\right)^3 (u^\alpha + \ell^\alpha) f_{\nu_e/\bar{\nu}_e}(k) \sigma_{\text{abs},\nu_e/\bar{\nu}_e}(k). \end{aligned} \quad (\text{B1})$$

The cross section of the absorption processes is written as

$$\sigma_{\text{abs},\nu_e/\bar{\nu}_e}(k) \approx \frac{(1 + 3g_A^2)G_F^2}{\pi} \omega^2, \quad (\text{B2})$$

where we ignored the electron mass and the difference between proton and neutron masses ($m_n - m_p \approx 1.293$ MeV). As in Eq. (A7), the energy deposition rates are evaluated in our scheme as

$$Q_{\text{abs},\nu_e}^{(+)\alpha} \approx \frac{(1 + 3g_A^2)G_F^2}{\pi} \langle\omega_{\nu_e}\rangle_{\text{abs}}^2 (Ju^\alpha + H^\alpha), \quad (\text{B3})$$

$$Q_{\text{abs},\bar{\nu}_e}^{(+)\alpha} \approx \frac{(1 + 3g_A^2)G_F^2}{\pi} \langle\omega_{\bar{\nu}_e}\rangle_{\text{abs}}^2 (\bar{J}u^\alpha + \bar{H}^\alpha). \quad (\text{B4})$$

Using these rates, the source terms for electrons (Eq.(11)) are written as

$$\mathcal{R}_{\text{abs},\nu_e} \approx \frac{Q_{\text{abs},\nu_e}^{(+)\alpha}(-u_\alpha)}{\langle\omega_{\nu_e}\rangle_{\text{abs}}} \approx \frac{(1 + 3g_A^2)G_F^2}{\pi} \langle\omega_{\nu_e}\rangle_{\text{abs}} J \quad (\text{B5})$$

$$\mathcal{R}_{\text{abs},\bar{\nu}_e} \approx \frac{Q_{\text{abs},\bar{\nu}_e}^{(+)\alpha}(-u_\alpha)}{\langle\omega_{\bar{\nu}_e}\rangle_{\text{abs}}} \approx \frac{(1 + 3g_A^2)G_F^2}{\pi} \langle\omega_{\bar{\nu}_e}\rangle_{\text{abs}} \bar{J}. \quad (\text{B6})$$

In the same way as Eq. (A11), we evaluate $\langle\omega\rangle_{\text{abs}}$ as

$$\langle\omega\rangle_{\text{abs}} = \frac{F_3(\eta_\nu)}{F_2(\eta_\nu)} T, \quad (\text{B7})$$

which means the average energy of neutrino assuming the Fermi-Dirac-type energy distribution.